Prediction of Small-Scale Cavitation in a High Speed Flow Over an Open Cavity Using Large Eddy Simulation

Ehsan Shams
Sourabh V. Apte*
Computational Flow Physics Laboratory
School of Mechanical Industrial and Manufacturing Engineering
Oregon State University, 204 Rogers Hall, Corvallis, OR 97331

Abstract

Large-eddy simulation of flow over an open cavity corresponding to the experimental setup of Liu and Katz [1] is performed. The filtered, incompressible Navier-Stokes equations are solved using a co-located grid finite-volume solver with the dynamic Smagorinsky model for subgrid scale closure. The computational grid consists of around seven million grid points with three million points clustered around the shear layer and the boundary-layer over the leading edge is resolved. The only input from the experimental data is the mean velocity profile at the inlet condition. The mean flow is superimposed with turbulent velocity fluctuations generated by solving a forced periodic duct flow at free-stream Reynolds number. The flow statistics, including mean and rms velocity fields and pressure coefficients, are compared with the experimental data to show reasonable agreement. The dynamic interactions between traveling vortices in the shear layer and the trailing edge affect the value and location of the pressure minima. Cavitation inception is investigated using two approaches: (i) a discrete bubble model wherein the bubble dynamics is computed by solving the Rayleigh-Plesset and the bubble motion equations using an adaptive time-stepping procedure, and (ii) a scalar transport model for the liquid volume fraction with source and sink terms for phase change. LES together with the cavitation models predict that inception occurs near the trailing edge similar to that observed in the experiments. The bubble transport model captures the subgrid dynamics of the vapor better, whereas the scalar model captures the large-scale features more accurately. A hybrid approach combining the bubble model with the scalar transport is needed to capture the broad range of scales observed in cavitation.

1 INTRODUCTION

The problem of cavitation has been widely studied owing to its influence on structural vibrations, noise production, erosion of propulsor blades, among others [2]. To devise strategies to

*Address all correspondence to this author. Email: sva@engr.orst.edu

avoid cavitation, it is necessary to predict its inception in unsteady turbulent flows. Rood [3] provides a review of different mechanisms of cavitation inception emphasizing that cavitation inception and turbulence are inseparable in many applications. Therefore, predictive numerical approaches (such as large-eddy simulations) for turbulent flows in complex flow configurations are necessary to accurately capture the inception process. However, modeling small-scale cavitation, cavitation inception and its unsteady evolution in engineering geometries is a challenging task. Liu and Katz [1] (henceforth referred to as LK2008) designed a well quantified experiment on high speed flow over an open cavity which can be used for detailed validation of the numerical approach in predicting cavitating flows in complex geometries as well as development and testing of subgrid scale models.

The cavitation number $[\sigma_i = (P_{ref} - P_v)/(0.5\rho_\ell U_\infty^2)]$, where P_v is the vapor pressure, ρ_ℓ is the liquid density, U_∞ is reference velocity, and P_{ref} is reference pressure value at which cavitation occurs, has typically been used to predict cavitation inception. If we assume that inception occurs when the pressure drops below vapor pressure, then a critical coefficient of pressure can be defined as $C_{p,min} = (P_{min} - P_{ref})/(0.5\rho U_\infty^2) = -\sigma_i$, where P_{min} is the minimum pressure within the domain. In turbulent flows, the location and the value of minimum pressure can change dramatically, and thus can affect the inception process. For high-speed flow over an open cavity, LK2008 showed that cavitation inception occurs above the trailing edge. However, they also observed a periodic variation in the amount of cavitation due to variations in pressure fields induced by the turbulent shear flow above the cavity.

Several numerical studies on cavitation inception have been performed for gaseous cavitation (i.e. growth of air micro-bubbles without significant transfer of mass from liquid to the bubble) [4, 5, 6, 7, 8, 9, 10, 11]. A majority of these studies used Reynolds-averaged Navier Stokes (RANS) models to predict cavitation inception. Recently, large-eddy simulation (LES) has also been used to study cavitation inception in a flow over a square cylinder [12]. A simple algebraic criterion for inception was developed based on stability of bubble nuclei to show good predictive capability of the LES methodology.

In the present work, LES of turbulent shear flow developing past an open cavity is performed to first investigate the predictive capability of LES with the dynamic Smagorinsky model [13]. Distribution of the coefficient of pressure (mean and rms) is used to identify cavitation inception regions over the trailing edge of the cavity and inside the shear layer. Cavitation inception is also studied by considering two types of models: (i) a discrete-bubble model (DBM) for gaseous cavitation based on the bubble-dynamics represented by Rayleigh-Plesset equation, and (ii) a scalar-transport model typically used for vaporous cavitation (involving phase change) [14, 15]. As the first step, the effect of the gaseous or vapor bubble dynamics on the fluid are neglected; that is the bubbles are assumed not to significantly affect the flow.

In the following sections, a brief overview of the mathematical formulation for the two models is presented. The discrete bubble model, involves computation and tracking of large number of bubble nuclei and can be expensive. An adaptive time-stepping scheme is developed and validated for efficient computation. These models are coupled with an LES solver and the results obtained are discussed in detail.

2 MATHEMATICAL FORMULATION

In this section, the mathematical formulation for the single-phase LES and the two-phase flow models are described. The three-dimensional, incompressible, filtered Navier-Stokes equations are written as

$$\frac{\partial \overline{u}_i}{\partial x_i} = 0 \tag{1}$$

$$\frac{\partial \overline{u_i}}{\partial t} + \frac{\partial \overline{u}_i \overline{u}_j}{\partial x_j} = -\frac{1}{\rho_\ell}\frac{\partial \overline{P}_\ell}{\partial x_i} + \nu_\ell \frac{\partial^2 \overline{u}_i}{\partial x_j x_j} - \frac{\partial \tau^r_{ij}}{\partial x_j}, \tag{2}$$

where τ^r_{ij} denotes the anisotropic part of the subgrid-scale stress tensor, $\overline{u_i u_j} - \overline{u}_i \overline{u}_j$, and the overbar indicates filtered variables, ν_ℓ is the kinematic viscosity and ρ_ℓ is the density of the liquid. The dynamic Smagorinsky model [13] is modified for unstructured grids and used for τ^r_{ij}. In Smagorinsky model, it is assumed that

$$q^r_{ij} = -2C\overline{\Delta}^2 |\overline{S}| \overline{S_{ij}}, \tag{3}$$

where q^r_{ij} is the aniostropic part of the subgrid scale stress ($\tau^r_{ij} = \overline{u_i u_j} - \overline{u}_i \overline{u}_j$), $\overline{S_{ij}}$ is the filtered strain-rate tensor, and $\overline{\Delta}$ is the filter width. Using least-squares approach for the dynamic procedure to compute the coefficient C yields,

$$C\overline{\Delta}^2 = -\frac{1}{2}\frac{M_{ij}L_{ij}}{M_{kl}M_{kl}}, \tag{4}$$

where

$$L_{ij} = \widehat{\overline{u}_i \overline{u}_j} - \widehat{\overline{u}}_i \widehat{\overline{u}}_j, \tag{5}$$

and

$$M_{ij} = \left(\widehat{\overline{\Delta}}/\overline{\Delta}\right)^2 \widehat{|\overline{S}|\overline{S_{ij}}} - \widehat{|\overline{S}|\overline{S_{ij}}}. \tag{6}$$

Here the test-filter is denoted by the symbol $\widehat{(\ )}$, and the ratio of the test to grid filter $\left(\widehat{\overline{\Delta}}/\overline{\Delta}\right)$ is commonly assumed to be 2. The filter width is defined as $V_{cv}^{1/3}$, where V_{cv} is the volume of the control volume and a top-hat test-filter is used based on the neighboring control volumes.

2.1 Discrete Bubble Model

The discrete-bubble model is based on an Eulerian-Lagrangian approach. A continuum description is used for the liquid phase with discrete Lagrangian tracking of the bubbles. The bubbles are usually treated as spherical point-particles with models for fluid-bubble interaction forces and bubble-bubble interactions. The bubble growth and collapse is modeled using the Rayleigh-Plesset equation [16, 6, 11]. Typically, in this type of discrete bubble model, small-size nuclei are assumed trapped inside the fluid. Existing nuclei or microbubbles may contain gas or vapor or a mixture of both. These nuclei may undergo rapid changes in size due to local pressure variations and can be used an as indicator of cavitation inception. The growth and collapse of bubbles can affect the fluid flow through momentum coupling as well

as through changes in bubble volume. In the present work we focus on cavitation inception, and do not consider the bubble-fluid coupling as well as effects of local void fraction variations [17]. The bubbles are thus simply tracked by solving the following equations for the bubble position ($\mathbf{x}_b$), velocity ($\mathbf{u}_b$), and radius (R_b):

$$\frac{\mathrm{d}}{\mathrm{dt}}(\mathbf{x}_b) = \mathbf{u}_b \tag{7}$$

$$m_b \frac{\mathrm{d}}{\mathrm{dt}}(\mathbf{u}_b) = \sum \mathbf{F}_b \tag{8}$$

$$\rho_\ell \left[R_b \frac{d^2 R_b}{dt^2} + \frac{3}{2}\left(\frac{dR_b}{dt}\right)^2 \right] = P_b - \overline{P}_{out} - \frac{2\sigma}{R_b} - \frac{4\mu_\ell}{R_b}\frac{dR_b}{dt} \tag{9}$$

where m_b is the mass, $\sum \mathbf{F}_b$ is the total force acting on the bubble, P_b and $\overline{P}_{out}$ are the pressures inside and outside of the bubble, respectively, σ is the surface tension coefficient, and μ_ℓ and ρ_ℓ are the liquid viscosity and density, respectively. To estimate P_b, it is typically assumed that the bubble contains some contaminant gas which expands or contracts according to adiabatic or isothermal processes [18, 19]. The pressure inside the bubble consists of contribution from the gas pressure (P_g) and the vapor pressure (P_v). The net bubble-pressure is computed as:

$$P_b = P_v + P_g = P_v + P_{g,0}\left(\frac{R_{b,0}}{R_b}\right)^{3\eta}, \tag{10}$$

where $P_{g,0}$ and $R_{b,0}$ are the reference partial pressure and bubble radius, respectively. For isothermal bubble expansion $\eta = 1$ whereas for an adiabatic expansion, $\eta = c_p/c_v$ (the ratio of specific heats of the gas at constant pressure and volume). The outside pressure $\overline{P}_{out}$ is taken as the pressure field interpolated to the bubble center location. Chahine and coworkers [6, 5] have shown that the bubble surface-averaged pressure (SAP) provides a better representation of the outside pressure. The net force acting on each individual bubble is given as [4]:

$$\sum \mathbf{F}_b = \mathbf{F}_G + \mathbf{F}_P + \mathbf{F}_D + \mathbf{F}_L + \mathbf{F}_{AM} + \mathbf{F}_{coll} + \mathbf{F}_{\dot{R}_b} \tag{11}$$

where $\mathbf{F}_G = (\rho_b - \rho_\ell)V_b\mathbf{g}$ is the gravitational force, $\mathbf{F}_P = -V_b\nabla P$ is the pressure force due to external pressure gradients, $\mathbf{F}_D = -\frac{1}{2}C_D\rho_\ell\pi R_b^2|\mathbf{u}_b - \mathbf{u}_\ell|(\mathbf{u}_b - \mathbf{u}_\ell)$ is the drag force, $\mathbf{F}_L = -C_L\rho_\ell V_b(\mathbf{u}_b - \mathbf{u}_\ell)\times\nabla\times\mathbf{u}_\ell$ is the lift force, $\mathbf{F}_{AM} = -\frac{1}{2}\rho_\ell V_b\left(\frac{D\mathbf{u}_b}{Dt} - \frac{D\mathbf{u}_\ell}{Dt}\right)$ is the added mass force, and $\mathbf{F}_{coll}$ is the inter-bubble or bubble-wall collision forces. The force $\mathbf{F}_{\dot{R}_b} = -4\rho_\ell\pi R_b^2(\mathbf{u}_b - \mathbf{u}_\ell)\frac{dR_b}{dt}$ represents momentum transfer due to variations in bubble size. Here, V_b and R_b are the bubble volume and radius, the subscripts 'b' and 'ℓ' correspond to the bubble and the fluid, respectively. Inter-bubble and bubble-wall interaction forces are computed using the standard collision models typically used in the discrete element method [20]. Several different models for the drag (C_D) and lift (C_L) coefficients have been proposed that account for bubble deformation and variations in bubble Reynolds numbers ($Re_b = \rho_\ell|\mathbf{u}_b - \mathbf{u}_\ell|2R_b/\mu_\ell$) [21]. The drag coefficient used in this study is given as:

$$C_D = \frac{24}{Re_b}(1 + 0.15Re_b^{0.687}).$$

The bubble dynamics is mainly governed by the outside pressure changes. In low pressure regions, the bubble size can vary rapidly and the Rayleigh-Plesset equations become very

stiff. An adaptive time stepping algorithm is used to efficiently solve for several bubble trajectories and still keep the overall computational time small [17, 22].

2.2 Scalar Transport Model

Eulerian-Eulerian two-phase models are also commonly employed in cavitation studies [14, 23, 15, 24]. These models usually are important for large-scale, vaporous-cavitation where a large region of the fluid flow consists of a cavity that can affect the fluid flow significantly. These models involve actual phase transition in regions where the local pressure drops below the vapor pressure. A scalar transport equation representing conservation of liquid mass, in terms of liquid volume fraction (Θ_ℓ), is solved. Source and sink terms in the scalar transport equation are used to model the phase change as [25, 15, 24],

$$\frac{\partial \Theta_\ell}{\partial t} + \nabla \cdot (\Theta_\ell \vec{u}) \;\; = \;\; \dot{m}^+ + \dot{m}^-, \tag{12}$$

where the source terms, $\dot{m}^-$ and $\dot{m}^+$, represent the destruction (evaporation) and production (condensation) of the liquid, respectively. They are both functions of the local and vapor pressures:

$$\dot{m}^- = \frac{C_{dest}\rho_\ell \min\left(P_\ell - P_v, 0\right)\Theta_\ell}{\rho_v \left(0.5\rho_\ell U_\infty^2\right) t_\infty}; \qquad \dot{m}^+ = \frac{C_{prod}\max\left(P_\ell - P_v, 0\right)\left(1-\Theta_\ell\right)}{\left(0.5\rho_\ell U_\infty^2\right) t_\infty}, \tag{13}$$

where C_{dest} and C_{prod} represent the empirical constants and t_∞ is the characteristic time-scale associated with the flow. In this work, C_{dest} and C_{prod} are set to 1.0 and 80, respectively, based on similar values used by Senocak & Shyy [25]. The time scale is set equal to the flow-through time based on the cavity length (L) and the mean flow velocity in the duct (U_∞).

To compare with the discrete bubble model, in the present work, we do not consider the pressure-velocity-density interactions through coupling the scalar transport model with the flow equations. Instead the dynamics of vapor production and destruction is simulated in a passive manner, similar to the 'one-way' coupling approach used in the discrete bubble model. This assumption is reasonable for small-scale cavitation where the local size of the vapor cavity is small as is the case in the present study.

3 COMPUTATIONAL APPROACH

An energy-conserving, finite-volume scheme for unstructured, arbitrarily shaped grid elements is used to solve the fluid-flow equations using a fractional step algorithm [26, 27, 28]. The velocity and pressure are stored at the centroids of the volumes. The cell-centered velocities are advanced in a predictor step such that the kinetic energy is conserved. The predicted velocities are interpolated to the faces and then projected. Projection yields the pressure potential at the cell-centers, and its gradient is used to correct the cell and face-normal velocities. A novel discretization scheme for the pressure gradient was developed by Mahesh *et al.* [26] to provide robustness *without numerical dissipation* on grids with rapidly varying elements. This algorithm was found to be imperative to perform LES at high Reynolds

number in complex flows. The overall algorithm is second-order accurate in space and time for uniform orthogonal grids. A numerical solver based on this approach was developed and shown to give very good results for both simple [29] and complex geometries [28] and is used in the present study. A thorough verification and validation of the algorithm was conducted [17] to assess the accuracy of the numerical scheme for test cases involving two-dimensional decaying Taylor vortices, flow through a turbulent channel and duct flows [17] and particle-laden turbulent flows [29, 28].

Scalar Transport: For the scalar-transport model, a scalar field is advected according to equation 12 using a third-order weighted, essentially non-oscillatory (WENO) scheme. The source terms in the scalar transport equation are treated explicitly, whereas the advection terms are treated implicitly.

Discrete Bubble Model: In the presence of large variations in the outside pressure, the bubble radius (R_b) and $\frac{dR_b}{dt}$ can change rapidly. Use of a simple explicit scheme with very small time-steps can be prohibitively expensive, even for a single bubble computation. An adaptive time-stepping strategy is necessary such that the bubble collapse and rapid expansion regions utilize small time-steps, but a much larger time-step can be used for relatively slow variations in bubble radius. An adaptive time step algorithm using the stability criteria of the solution is developed. The stability criterion is based on the eigenvalues of the ODEs (equation 7). Detailed verification of the model for bubble motion in complex flows has been conducted to show second-order accuracy [17].

4 NUMERICAL SETUP

The numerical setup consists of a straight ducted channel with a nearly square cavity in the central region as shown in figure 1. The duct in the computational domain starts at -12.4 mm before the cavity leading edge and ends at 32 mm after the trailing edge. The duct height is 33.5 mm in the experimental setup. The geometry parameters, flow conditions, and grid resolutions used are summarized in table 1. Emphasis of the present work is on the shear layer and the leading and trailing edges of the cavity, thus, refined grids are used in these regions. The grid elements are mainly Cartesian hexahedra with refined regions in the leading edge and near wall regions. The boundary-layers in the leading and trailing edges are resolved.

In the present simulation, the boundary layers are resolved, and no-slip conditions are applied at walls. In order to keep the computational size small, we simulate only a portion of the duct in the y-direction and apply slip condition at the top boundary. Since the duct height is very large, the top surface condition has little effect on the shear-layer development. A convective outflow boundary condition is applied at the outlet. In the experiments, the flow is tripped by thirteen notches upstream of the duct and then passed through a converging section [1]. The divergent section is not simulated in the present study. Instead, it is assumed that the flow is fully developed and the experimentally measured mean velocity field is used as inlet condition. In LES, to create proper turbulence structure and velocity fluctuations, it is important to impose consistent fluctuations in the velocity field at the inlet [30]. Use of random fluctuations scaled with turbulence intensity values; however, can lead to convergence issues in a conservative numerical solver. A separate periodic duct

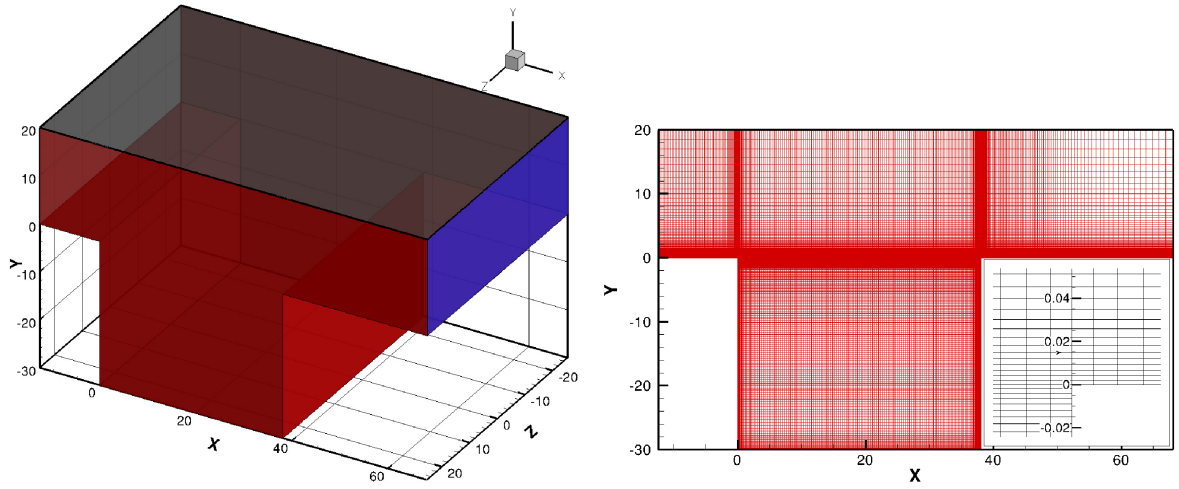

(a) 3D View

(b) $Z = 0$, Centerplane

Figure 1: Computational domain and grid: (a) three-dimensional domain with Cartesian grid, (b) refined grids (dimensions shown are in mm) are used in the shear layer and near the cavity leading and trailing edges. A zoomed-in view of the grid near the trailing edge is shown in wall co-ordinates.

Table 1: Cavity geometry and computational grid (+ denotes wall units, $y^+ = yu_\tau/\nu$. $u_\tau \approx 0.42$ at a point upstream of the leading edge). Base grid is refined in all directions compared to coarse grid. Fine grid is refined in spanwise direction compared to base grid.

Geometry and parameters	Cavity size	$38.1 \times 30 \times 50.8$ mm^3
	Duct size	$92.4 \times 20 \times 50.8$ mm^3
	Cavity length L	38.1 mm
	Average inflow velocity, U_∞	5 m/s
	Reynolds number $Re_L = \frac{U_\infty L}{\nu}$	170,000
coarse grid	$\Delta x_{min} = \Delta y_{min}$, $\Delta x^+_{min} = \Delta y^+_{min}$	3.8 μm, 1.3
(6×10^5)	Δz, Δz^+	1000 μm, 348
base grid	$\Delta x_{min} = \Delta y_{min}$, $\Delta x^+_{min} = \Delta y^+_{min}$	1.9 μm, 0.67
(5×10^6)	Δz, Δz^+	500 μm, 174
fine grid	Δy_{min}, Δy^+_{min}	2.0 μm, 0.7
(7×10^6)	Δz, Δz^+	200 μm, 69

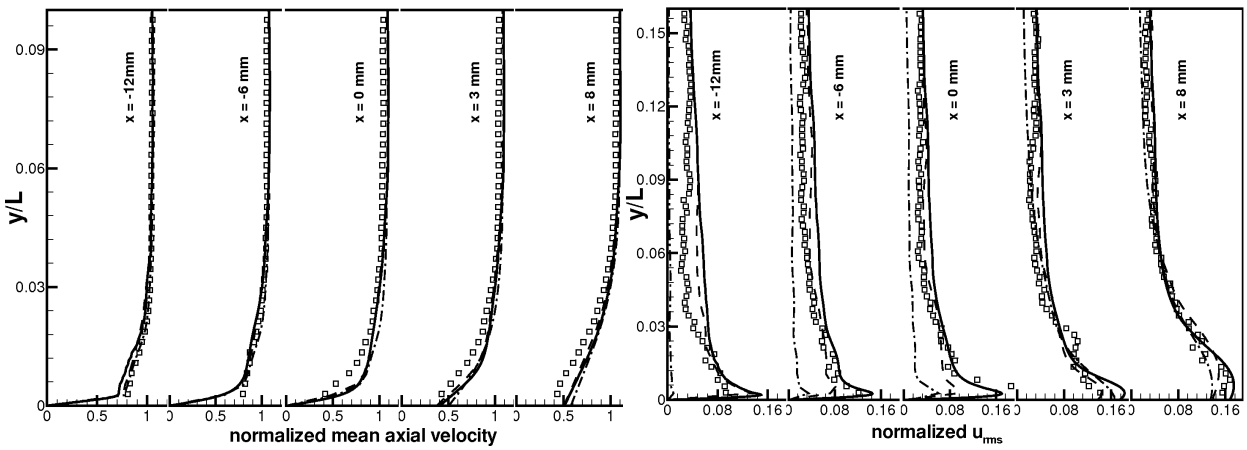

Figure 2: Comparison of mean and *rms* axial velocity variations in the vertical direction with experimental data of LK2008: results from fine (solid line), base (dotted lines), coarse grid (dashed line), and experiment (symbols) are shown. Inlet fluctuations are enforced only in the base and fine grids.

flow is simulated at the desired mass-flow rate and Reynolds number using a body-force technique [30]. The Reynolds number based on the friction velocity for the inflow duct and duct half height is very high ($Re_\tau = 8900$) and performing a full DNS of periodic duct flow is beyond the scope of this study. In order to get reasonable levels of turbulence intensity at the inlet, we performed an LES of a periodic flow in a full-duct on $180 \times 256 \times 144$ grid points with the resolution of $\Delta x^+ = 64$, $\Delta z^+ = 42$, and $\Delta y^+_{min} = 0.835$, $\Delta y^+_{max} = 85$ (where the superscript '+' denotes wall variables). The resolution is fine in the wall-normal and axial directions; however, coarse in the spanwise direction. This resolution was used in order not to increase the simulation size for the inlet conditions considerably. Instantaneous velocity fluctuations obtained from the turbulent duct flow calculation is stored at the inlet plane over a long period of time. These fluctuations are then read at each time-step of the actual cavity simulation and interpolated to the computational grid at the inlet plane. The velocity fluctuations are then added to the experimental mean velocity profile and used as an inlet condition.

In order to verify that the inlet conditions are properly represented in the present simulation, the mean and *rms* velocity fields are compared with the experimental data in the turbulent boundary layer upstream of the leading edge as well as downstream in the shear layer. Figure 2 shows comparison of the vertical variations in the mean and *rms* axial velocity near the leading edge with the data from LK2008. In order to assess the importance of inlet fluctuations, only the base and fine grid calculations included the inlet fluctuations. The coarse grid, however, used the mean experimental velocity profile as inlet condition without any fluctuations. Figure 2 shows that mean flow predicted by all grids agrees with the experiments reasonably. The *rms* axial velocity field is also captured well by the base and fine grid simulations. The coarse grid without any inlet fluctuations, does not show any turbulence intensity levels upstream of the leading edge, but shows reasonable levels in the shear layer $x > 0$).

5 NUMERICAL RESULTS

We first compare the flow statistics obtained from the simulation, including mean and *rms* values of the flow field, to those reported in LK2008. Detailed comparisons of flow statistics between LES and experimental data are presented. Small scale cavitation studies based on discrete bubble and scalar transport models are presented next.

5.1 Velocity and Pressure Statistics

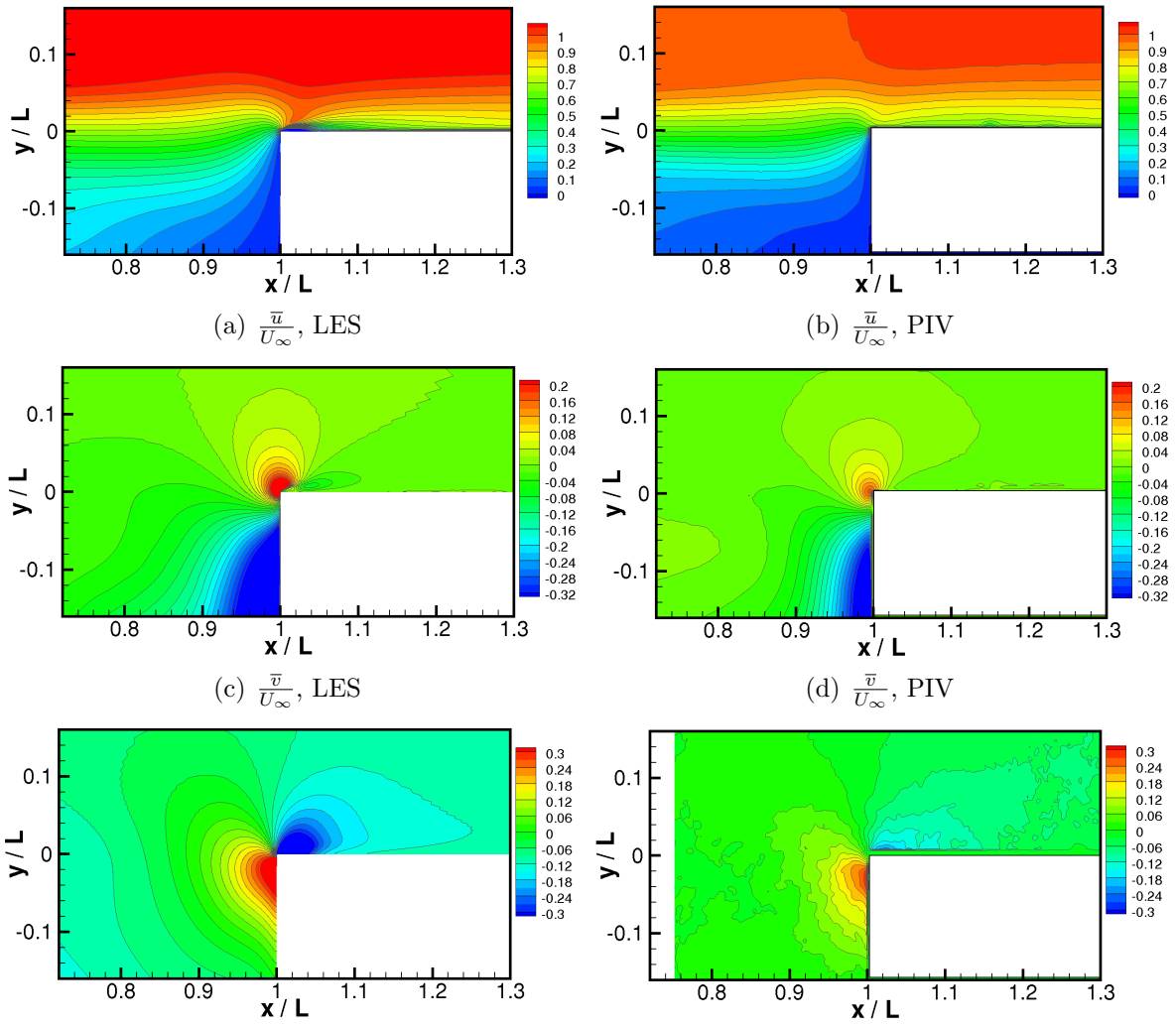

(a) $\frac{\overline{u}}{U_\infty}$, LES (b) $\frac{\overline{u}}{U_\infty}$, PIV

(c) $\frac{\overline{v}}{U_\infty}$, LES (d) $\frac{\overline{v}}{U_\infty}$, PIV

(e) $\overline{C}_p$, LES (f) $\overline{C}_p$, PIV

Figure 3: Contours of mean velocity and C_p fields near the trailing edge compared with corresponding PIV data of LK2008.

Contour plots of the normalized mean axial, vertical velocity, and pressure coefficient ($\overline{C}_p$) compared with the time-averaged PIV data are presented in figure 3. The distribution of the mean velocity field is very similar to that shown by LK2008. It is observed from the mean streamlines that the shear layer impinges the trailing edge slightly below the corner. The LES results predict the behavior of the mean axial and vertical velocity reasonably well near the trailing edge. The distribution of the mean pressure near the trailing edge

is also shown in figure 3. The following two features also observed in the experiments are accurately predicted: (i) a high-pressure region just upstream of the trailing edge (corner in the present 2D plane) which extends into the cavity, and (ii) a low pressure region above the trailing edge. The high pressure region just upstream of the trailing edge occurs due to the impingement of the shear layer onto to the trailing edge, creating a stagnation point slightly below the edge. The sharp corner, just downstream of the stagnation point, causes low pressure region above the trailing edge. The size of the low and high pressure region very close to the trailing edge is slightly larger than that observed in experiments; however, the shape of contours of $\overline{C}_p$ are similar to those observed in the experiments. The actual values of $\overline{C}_p$ predicted by LES are higher right at the impingement point and above the trailing edge.

Figure 4 compares the contours of turbulence intensities and Reynolds stress with the experimental data. Above the trailing edge, there is small recirculation region observed in the LES studies that is not captured by the PIV data. The mean vertical velocity contours at the trailing edge are also slightly higher compared to the PIV data. Figure 5 shows vertical variations in axial rms velocity and Reynolds stress at different axial locations near the trailing edge for three-different grid resolutions. With grid-refinement, the statistics show improved predictions in comparison to the experimental data.

The turbulence intensities and Reynolds stresses are reasonably well predicted close to the trailing edge, but show higher values in a small region slightly above the trailing edge. This may be related to the dynamic subgrid scale viscosity variations in this region involving complex flow patterns. The dynamic subgrid scale model used in this work, requires averaging in homogeneous directions for the Smagorinsky constant. In our computation, only a local averaging was implemented since the flow is developing behind the trailing edge. With grid-refinement, this averaging is done on a smaller region and perhaps may contribute to the over-prediction. It also affects the variation in subgrid viscosity, and this suggests that a careful analysis of subgrid-scale LES models is necessary in this region. In addition, the grid refinement in the present work is mainly done in the spanwise direction. The wall-normal and the span-wise grids are fine near the wall, this gives very high aspect ratio grid cells close to the wall. This may also influence the behavior of the turbulence quantities near the wall. A better distribution of the grid elements in the entire domain reducing the aspect ratio of grid cells near the wall may improve the predictions.

The probability distribution functions (PDFs) of the fluctuations in pressure coefficient (C'_p) at the eight probes (p1–p8) are shown in figure 6 together with location of probes in the center plane as shown on the $\overline{C}_p$ contours. The corresponding mean and rms values of C_p are also quoted. Probes p1 and p2 are slightly upstream of the trailing edge, probes p3 and p4 are in the shear layer, and probes p5–p8 are downstream of the trailing edge. Based on the mean values of C_p and the PDFs of C'_p, cavitation is likely to occur inside the shear layer for a cavitation index of $\sigma_i \leq\sim 0.43$ (for example, for probe p3, $\overline{C}_p = -0.13$ with a PDF tail of around -0.3). LK2008 also observed cavitation inside the shear layer for similar inception index. The mean statistics were collected over twelve flow through times, where one flow through time is taken to be approximately L/U_∞.

The probes (p5–p8) above the trailing edge (downstream of the corner) show low values of $\overline{C}_p$ together with a broader spectrum of C'_p. Inception first occurs inside these regions as

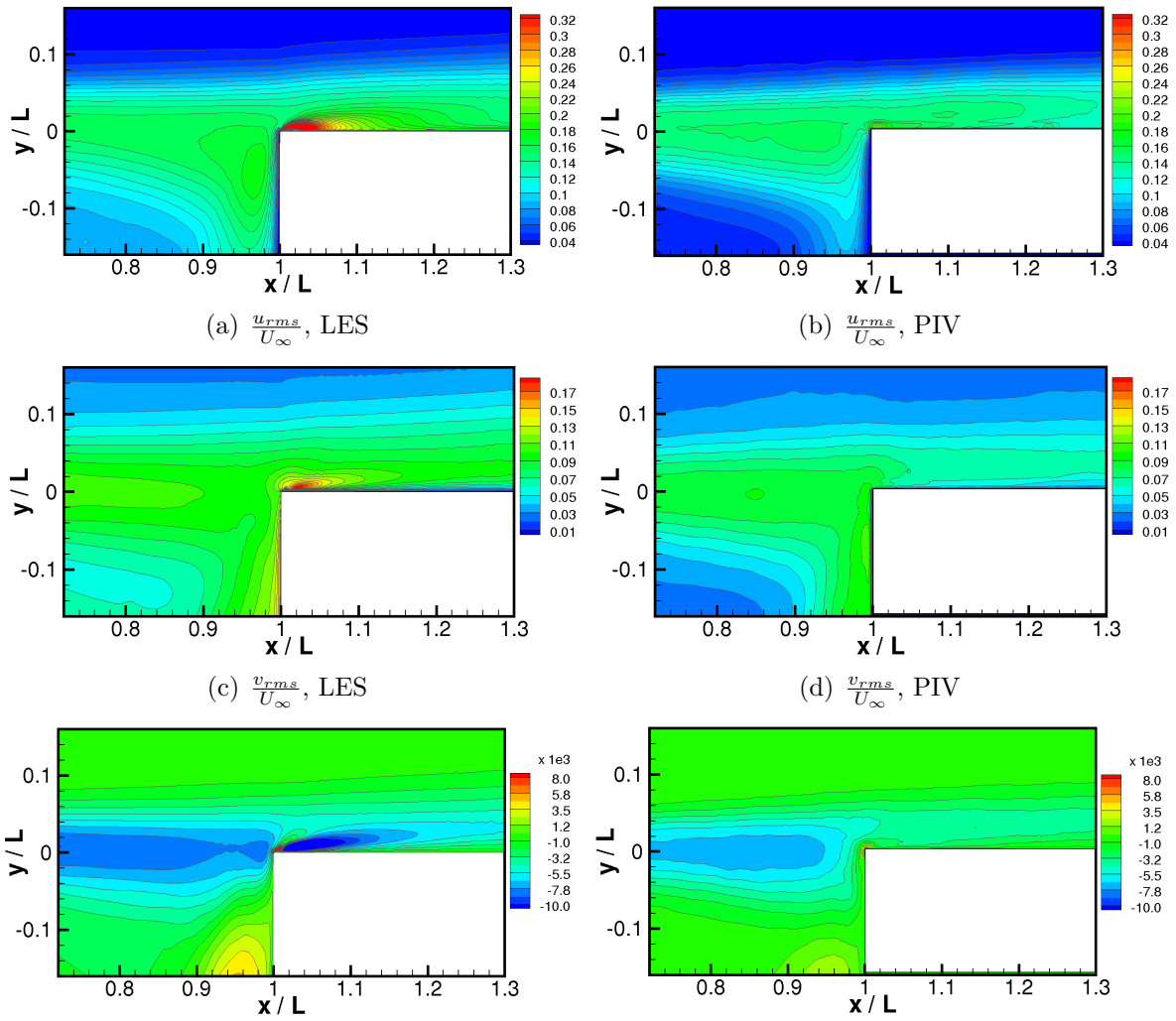

(a) $\frac{u_{rms}}{U_\infty}$, LES

(b) $\frac{u_{rms}}{U_\infty}$, PIV

(c) $\frac{v_{rms}}{U_\infty}$, LES

(d) $\frac{v_{rms}}{U_\infty}$, PIV

(e) $\frac{\overline{u'v'}}{U_\infty^2}$, LES

(f) $\frac{\overline{u'v'}}{U_\infty^2}$, PIV

Figure 4: Contours of axial and vertical *rms* velocity fields as well as Reynolds stress compared with PIV data of LK2008 near the trailing edge.

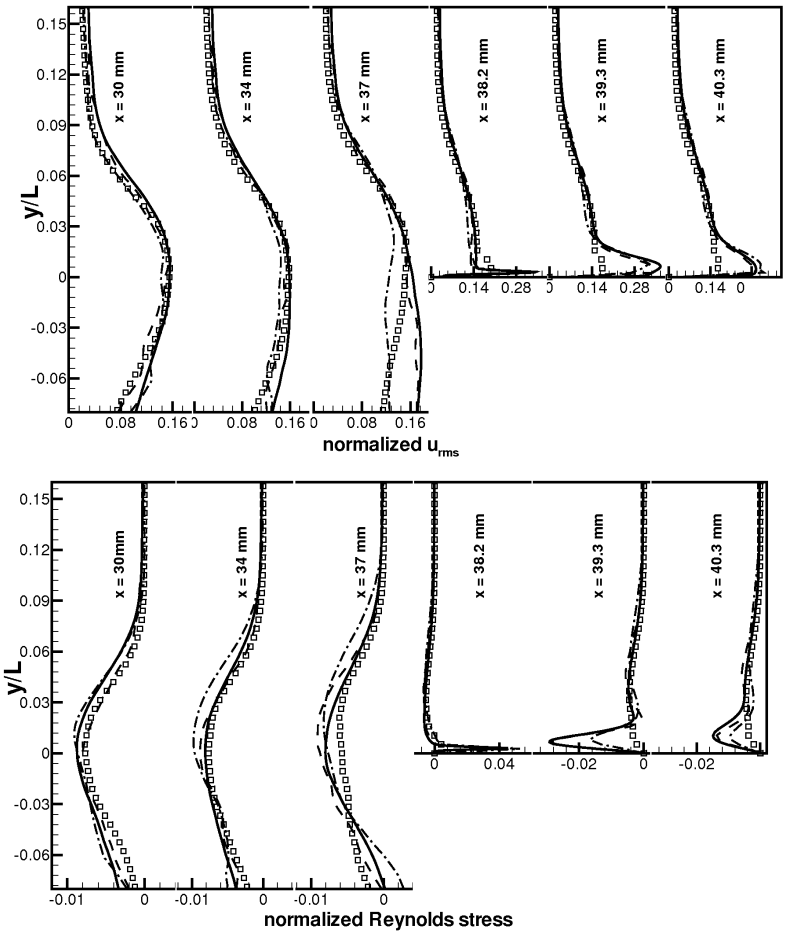

Figure 5: Vertical variations of normalized rms velocity ($\frac{u_{rms}}{U_\infty}$) and Reynolds stress ($\frac{\overline{u'v'}}{U_\infty^2}$) near the trailing edge: fine grid (solid line), base grid (dotted lines), coarse grid (dashed line), experiment data (symbols).

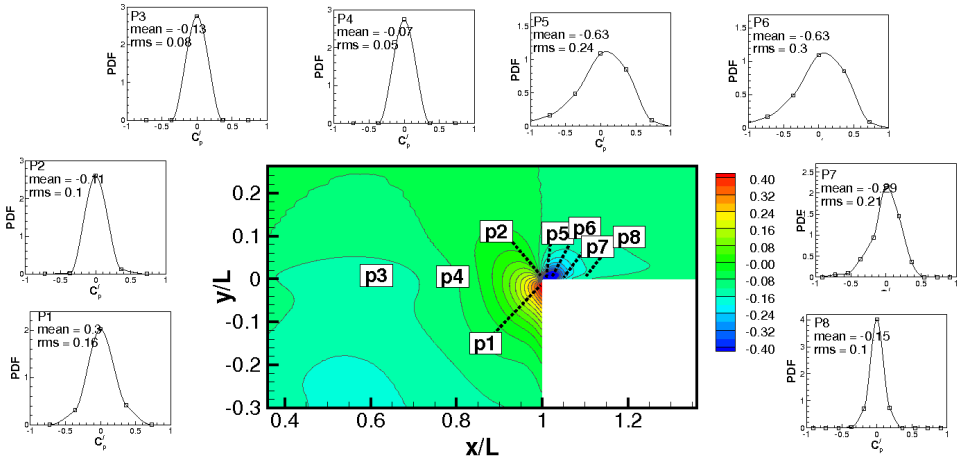

Figure 6: Probability distribution functions for C_p' at the eight probe locations (p1–p8) shown in contour plot of $\overline{C}_p$.

also noted by LK2008. It is observed that in the present simulations, the absolute values of mean pressure coefficient ($|\overline{C}_p|$) at some points above the trailing edge (i.e. probes p5–p8) were generally higher and the rms values ($C_{p,rms}$) were lower compared to the experimental data. For example, at probe p6, $\overline{C}_p = -0.63$ and $C_{p,rms} = 0.3$ providing an inception index of $\sigma_i = 0.93$. LK2008 also reported inception index of $\sigma_i = 0.9$; however, generally showed lower $\overline{C}_p$ and higher C'_p above the trailing edge. In LES, the PDFs of C'_p showed larger negative tails. If instantaneous values of C_p are used as criterion for inception, these distributions indicate that inception above the trailing may occur at even higher σ_i values. In experiments, the pressure signal was deduced based on the material acceleration $D\mathbf{u}/Dt$ by neglecting the viscous effects [31]. In LES, near the trailing edge, the viscous effects may be small; however, the subgrid-scale stresses can be large influencing the filtered pressure field as:

$$-\frac{1}{\rho_\ell}\nabla\overline{P} = \frac{D\overline{\mathbf{u}}}{Dt} + \frac{\partial\tau^r_{ij}}{\partial x_j}. \tag{14}$$

It is conjectured that local variations in subgrid-scale viscosity (and hence stresses) obtained from the dynamic model may affect the filtered pressure field resulting in lower pressure values in a small region above the trailing edge. The variations in C_p values above the trailing edge were related to the impacting of shear layer vortices on the trailing edge and is discussed below. It was observed in the simulations that, near the trailing edge corner, the eddy viscosity obtained from the dynamic Smagorinsky model requires clipping relatively frequently [17].

5.2 Instantaneous Flow Field

Figure 7 shows the instantaneous plots of $C_p = (P-P_\infty)/(0.5\rho U^2_\infty)$ in the center plane (z = 0) together with instantaneous streamlines obtained by removing $0.5U_\infty$ from the axial velocity field. Low pressure regions within the shear layer and corresponding vortical structures are clearly visible. The two snapshots (7a,b) correspond to higher and lower pressures just above the trailing edge corner (x/L = 1.01, y/L = 0.0035, z/L = 0). The vortical structures in the shear layer generated from the leading edge separation travel downstream and interact with the trailing edge causing significant changes in the C_p values above the trailing edge. Liu and Katz [1] showed similar vortex structures and argued that there is a strong correlation between the traveling vortices and the trailing edge, causing flow-induced C_p fluctuations.

In order to analyze the frequency of shear-layer vortices impinging on the trailing edge, pressure probe was placed on the vertical wall of the trailing edge inside the cavity region ($x/L = 0.98, y/L = -0.26,\ z/L = 0$), at a location close to the probe measurements performed by Liu and Katz [1]. Figure 7d shows the power-spectral density of C_p as observed by this probe versus Strouhal number, $St = fL/U_\infty$ where L is length of the cavity and ($U_\infty = 5$ m/s) is the mean inlet velocity. The probe shows peaks at Strouhal numbers 1.37 ($f = 180$ Hz) and 0.8 ($f = 105$ Hz). Experimental data showed peaks at 90 and 160 Hz. Theoretical predictions of frequency of shedding vorticies in the shear layer based on the mean convection speed of the vorticies [32, 33] provide the following analytical expression for the Strouhal number,

$$St = \frac{fL}{U_\infty} = \frac{c}{U_\infty}\left(n + \frac{1}{4}\right) \tag{15}$$

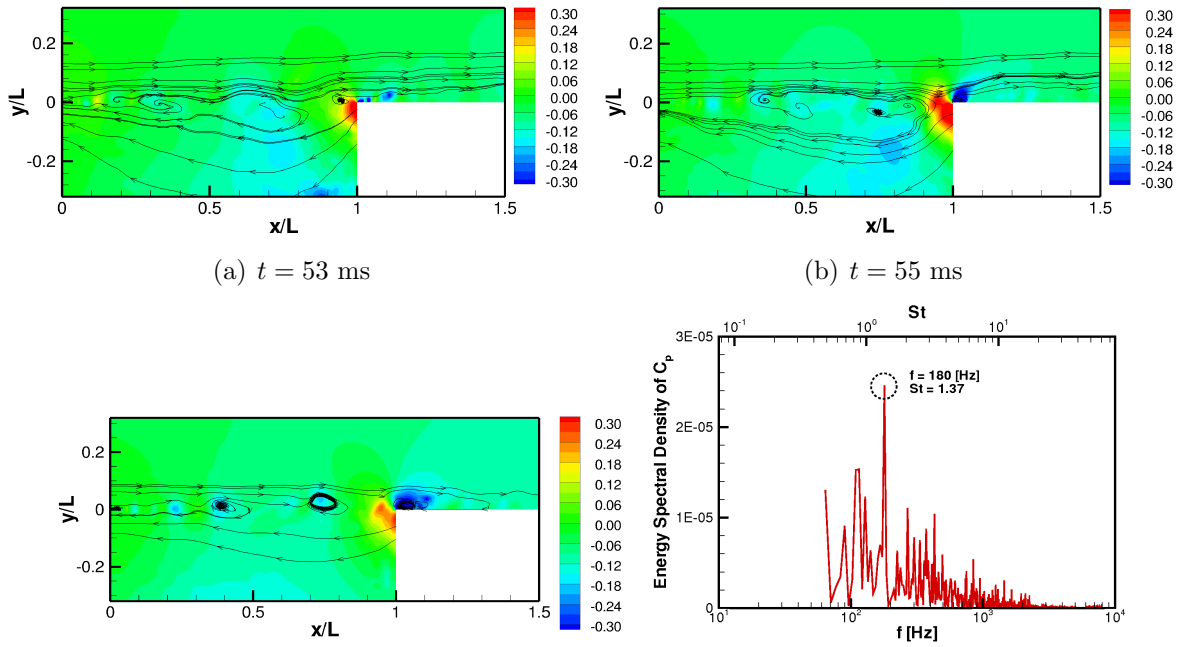

(a) $t = 53$ ms (b) $t = 55$ ms

(c) $t = 65$ ms (d) PSD of C_p

Figure 7: Instantaneous pressure contours and stream traces (based on removing $0.5U_\infty$ from the streamwise velocity):(a) $t = 53$ ms (high pressure above the trailing edge), (b) $t = 55$ ms (low pressure above the trailing edge), (c) $t = 65$ ms, (d) power spectral density of C_p at a probe near the vertical wall of the trailing edge ($x/L = 0.98, y/L = -0.26$, $z/L = 0$).

where c is the convection speed, L is the length of the cavity, $n = 2$ corresponds to simultaneous presence of two vorticies in the shear layer. If we take $c/U_\infty = 0.5$, the theoretical value for frequency for the present case studied is 147 Hz and the corresponding Strouhal number is 1.125. For $n = 1$, the corresponding values are 82 Hz and $St = 0.67$. The LES predictions show slightly higher Strouhal numbers, but are on the same order as the experiments and the theoretical analysis. This also indicates the correct convection speed of the vortices traveling and impinging onto the shear layer as close to half of the free-stream velocity. Furthermore, Liu and Katz [1] show a frequency of 300-320 Hz ($St = 1.22$) for the case with $U_\infty = 10$ m/s (twice as much as that used for the present simulation). Based on this, our frequency of cavitation above the trailing edge is well predicted. Additional, spectral analysis of the C_p signal above the trailing edge (where cavitation inception occurs) is presented in the next section.

At the above location, the C_p value varies over a wide range -0.01 to -2. The C_p values also showed variations in the spanwise directions suggesting that the impact location of the vortex cores on the trailing edge (and the stagnation point) move in and out of the plane (in spanwise directions). Based on the mean and rms values of the pressure coefficient at neighboring points ($\overline{C}_p \sim -0.639$, $C_{p,rms} \sim 0.29$), the inception index is approximated as, $\sigma_i \sim 0.93$.

5.3 Small Scale Cavitation and Inception

We consider two different approaches to investigate the nature of small-scale cavitation near the trailing edge and inside the shear layers: (i) a scalar transport model and (ii) a discrete bubble model. The results obtained from these two models are described below.

Scalar Transport Model: For the scalar-transport model, a transport equation for liquid volume fraction (equation 12) is solved as described earlier. The source and sink terms in the transport equation are proportional to the difference between the local pressure and the vapor pressure as well as the amount of liquid present in a given control volume. Typically, if the local pressure drops below the vapor pressure, the liquid evaporates creating vapor. In the present work, the local pressure field was defined relative to the pressure field above the leading edge of the cavity (P_∞). Similarly to the experiments, the absolute value of P_∞ was reduced starting with one atmosphere. The vapor pressure was assumed to be $P_v = 2.337$ kPa. Initially, a uniform vapor of $\phi = 1 - \Theta_\ell = 10^{-5}$ is assumed distributed over the computational domain. This is based on the dissolved gas concentration estimated in LK2008 for the present case.

Early sites of cavitation were observed above the trailing edge where the pressure minima occur. Small amounts of vapor were created in this region with vapor fractions on the order of 0.01 for a cavitation index of $\sigma_i = 0.9$.

Figures 8a,b show the temporal variation of vapor fraction ($\phi = 1-\Theta_\ell$) and C_p just above the trailing edge at two different upstream pressure levels. As can be seen from the time traces, periodic occurrence and disappearance of cavitation is predicted above the trailing edge. The pressure variations are mainly caused by the shear-layer eddies impinging on the the cavity trailing edge (see figures 7).

For pressures corresponding to the cavitation index of $\sigma_i = 0.9$, the inception of small-scale cavitation was observed. Further reduction in P_∞ resulted in increased amount of cavitation above the trailing edge. In the experiments, vigorous cavitation was observed for $\sigma_i = 0.4$. Figures 8c,d show the power-spectral density of the pressure coefficient (C_p) and the scalar (ϕ) above the trailing edge for $\sigma_i = 0.4$. Strong peaks are observed at the frequency of 139 Hz and 143 Hz for C_p and ϕ, respectively. Liu and Katz [1] observed periodic cavitation at frequencies 300-350 Hz for the case of twice the free-stream velocity (10 m/s). For half the free-stream velocity considered here, the convective speed of traveling vorticies is halved. Power spectra of C_p presented earlier show similar range of periodic frequency for the vortices impinging on the trailing edge.

In the present work, we do not have pressure-velocity-density coupling, which may become important when heavy cavitation occurs (for the case of $\sigma_i \leq 0.4$). However, the features associated with periodic growth and decay of the vapor fraction above the trailing edge are captured. For this scalar transport model, the local vapor fraction did not exceed unity; however, larger values of ϕ were observed especially with lower upstream pressures. Pressure-velocity-density coupling may become important under these vigorous cavitation stages and will be part of a subsequent study.

We decreased the upstream pressure in the scalar transport studies to give $\sigma_i = 0.1$. For this case, cavitation also occurred in the shear layer above the cavity with periodic appearance and disappearance above the trailing edge. The amount of vapor on the shear layer is mainly generated due to pressure being lower than vapor pressure or $C_p < \sigma_i = 0.1$.

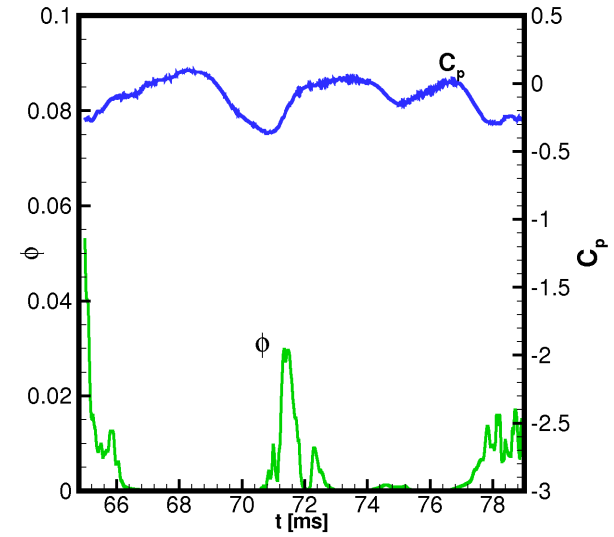

(a) $\vec{\mathbf{x}} = (38.0, 0.3, 0.0)$, $\sigma_i = 0.9$

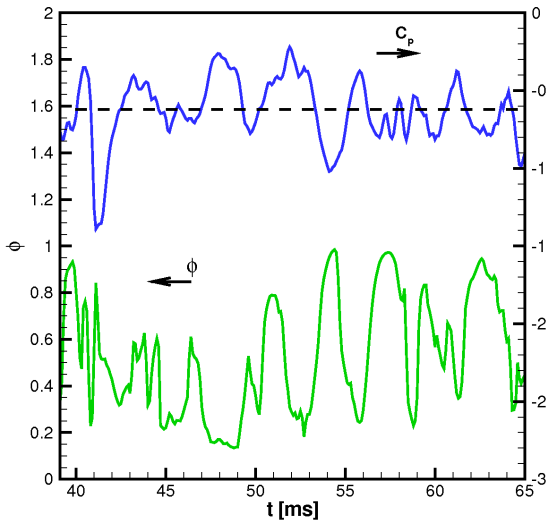

(b) $\vec{\mathbf{x}} = (38.1, 0.01, 0.0)$, $\sigma_i = 0.4$

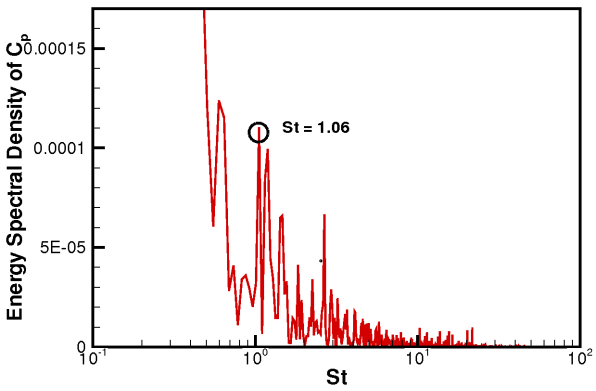

(c) $\vec{\mathbf{x}} = (38.1, 0.01, 0.0)$, $\sigma_i = 0.4$

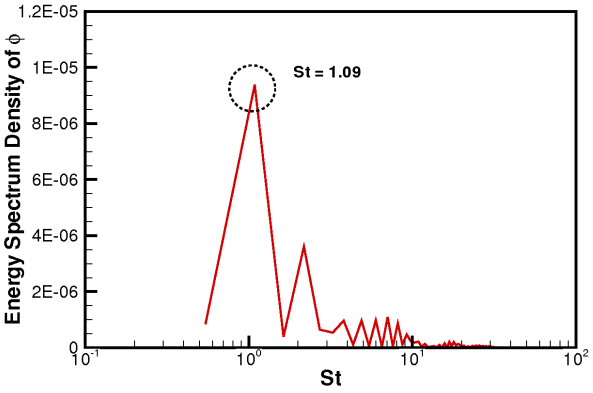

(d) $\vec{\mathbf{x}} = (38.1, 0.01, 0.0)$, $\sigma_i = 0.4$

Figure 8: Time evolution of vapor fraction and C_p near the trailing edge: (a) for $\sigma_i = 0.9$ at $\vec{\mathbf{x}} = (38.0, 0.3, 0.0)$, and (b) for $\sigma_i = 0.4$ and $\vec{\mathbf{x}} = (38.1, 0.01, 0.0)$, (c) power spectral density of C_p and (d) power spectral density of ϕ for $\sigma_i = 0.4$.

Liu & Katz [1] also observed vapor bubbles and cavitation in the shear layer for $\sigma_i < 0.4$.

Discrete Bubble Model:

We also performed cavitation inception studies using the discrete bubble model (DBM). The gas content in the liquid was assumed to be small (initial gas void fraction was assumed to be 10^{-5} based on LK2008). It is important for the bubble nuclei to pass through the low pressure regions above the cavity ('window of opportunity' to get drawn into low pressure regions and cavitate) [6]. Accordingly, air nuclei were distributed evenly in a small band around the shear layer. The bubbles were initially injected over a small region in the streamwise direction and in a band of 10 mm in the mid section of flow span. In order to keep the number of bubbles constant in the domain, bubbles were continuously injected near the leading edge and removed further downstream from the trailing edge. To analyze the sensitivity of the initial bubble size to cavitation inception, detailed PDF analysis (following the works of Cerutti *et al.* [8] and Kim *et al.* [9]) was performed.

Table 2: Case studies to analyze cavitation inception using the Discrete Bubble Model.

Case	Figure Symbol	d_{initial} (μm)	σ_i
C1	square	10	0.4
C2	triangle	50	0.4
C3	circle	100	0.4
C4	diamond	50	0.9
C5	circle (filled)	50	1.4
C6	square (filled)	50	0.1

The initial pressure inside the bubble was set based on an equilibrium radius corresponding to the radius of the nuclei and its location in the domain. Using the Rayleigh-Plesset equation at equilibrium conditions, the pressure inside the bubble can be obtained as: $P_b = \overline{P}_{out} + 2\sigma/R_b$ (σ is the surface tension coefficient). The bubbles are then advected with 'one-way' coupling (bubbles do not affect the flow). On an average, approximately $50,000$ bubble trajectories are tracked at each instant. In order to gain better understanding of how different parameters such as the initial bubble size and cavitation index σ_i affect the inception and the behavior of bubbles, three different initial bubble sizes (10, 50, and 100 μm) were considered with a constant cavitation index ($\sigma_i = 0.4$). In addition, four different cavitation indices (0.1, 0.4, 0.9, and 1.4) were examined on a certain initial bubble diameter ($d_{init} = 50$ μm). Table 2 shows different diameters and cavitation indices used in the present study. Figure 9 shows the temporal evolution of bubble locations inside the shear layer and above the trailing edge. The size of the scatter symbols is scaled with respect to the size of the bubble. Accordingly, large size bubbles are obtained near the trailing edge. For $\sigma_i = 0.4$ large size bubbles are readily observed near the trailing edge. As shown later, for this inception index, bubbles inside the shear layer showed the most growth, and rapid variation in bubble size occurs near the trailing edge. For higher pressure at the upstream ($\sigma_i = 0.9$), bubbles cavitate near the trailing edge; however, little change in size of the bubbles was observed inside the shear layers.

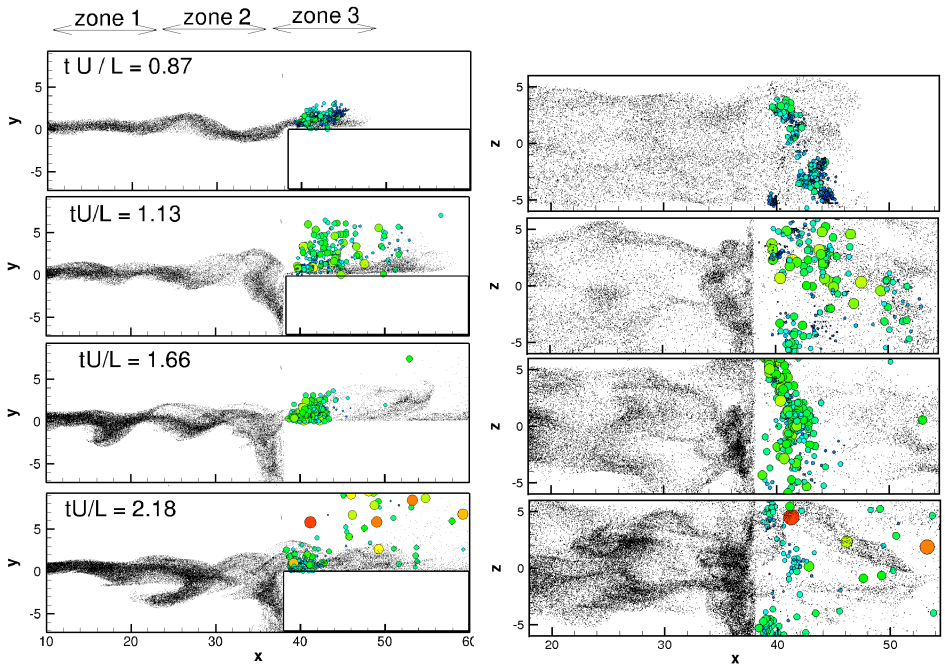

(a) side view (b) top view

Figure 9: Temporal evolution of bubble distribution (initial size 50 μm) on the shear layer for $\sigma_i = 0.4$ during the initial stages: (a) side view showing entire shear layer and trailing edge, (b) top view above the trailing edge.

Data Sampling: To analyze the effect of various model parameters, we computed probability distribution functions (PDFs) of number of bubbles based on their growth ratio d/d_{initial}, the pressure coefficient C_p, and the vorticity ω at bubble position. Three different initial bubble sizes were considered (cases C1, C2, C3), and for initial bubbles of 50 μm the cavitation index was varied (σ_i = 0.4, 0.9, 1.4, and 0.1) in cases C2, C4, C5, and C6. In addition, we looked at different regions in the flow near the leading edge (zone 1), in the mid-section (zone 2) and over the trailing edge (zone 3) as shown in figure 9. The extent of these zones in the vertical direction is $-5\text{mm} < y < 5\text{mm}$. In the stream-wise direction the zones are defined as: $-2\text{mm} < x < 25\text{mm}$ (zone 1), $25\text{mm} < x < 38\text{mm}$ (zone 2), and $38\text{mm} < x < 45\text{mm}$ (zone 3). We have also performed conditional sampling on the parameters based on bubble growth ratio (d/d_{initial}), and location. For the conditional PDF based on growth ratio, we defined three different zones of $d/d_{\text{initial}} < 0.8$, $0.8 < d/d_{\text{initial}} < 1.25$, and $1.25 < d/d_{\text{initial}}$, referred to as small, medium, and large. For the PDF calculations, data (minimum to maximum of each parameter) have been divided into 41 different bins which are distributed logarithmically for diameter and linearly for pressure and vorticity. Samples collected over several instantaneous snapshots were averaged and these results are discussed below.

Effect of Cavitation Index: Figure 10 shows the effect of cavitation index on the PDFs and number of bubbles sampled based on the bubble growth ratio (d/d_{initial}) and the pressure at the bubble location in various regions of the shear layer and the trailing edge. These plots are obtained with fixed initial bubble size of 50 μm. In figure 10(a) we observe that

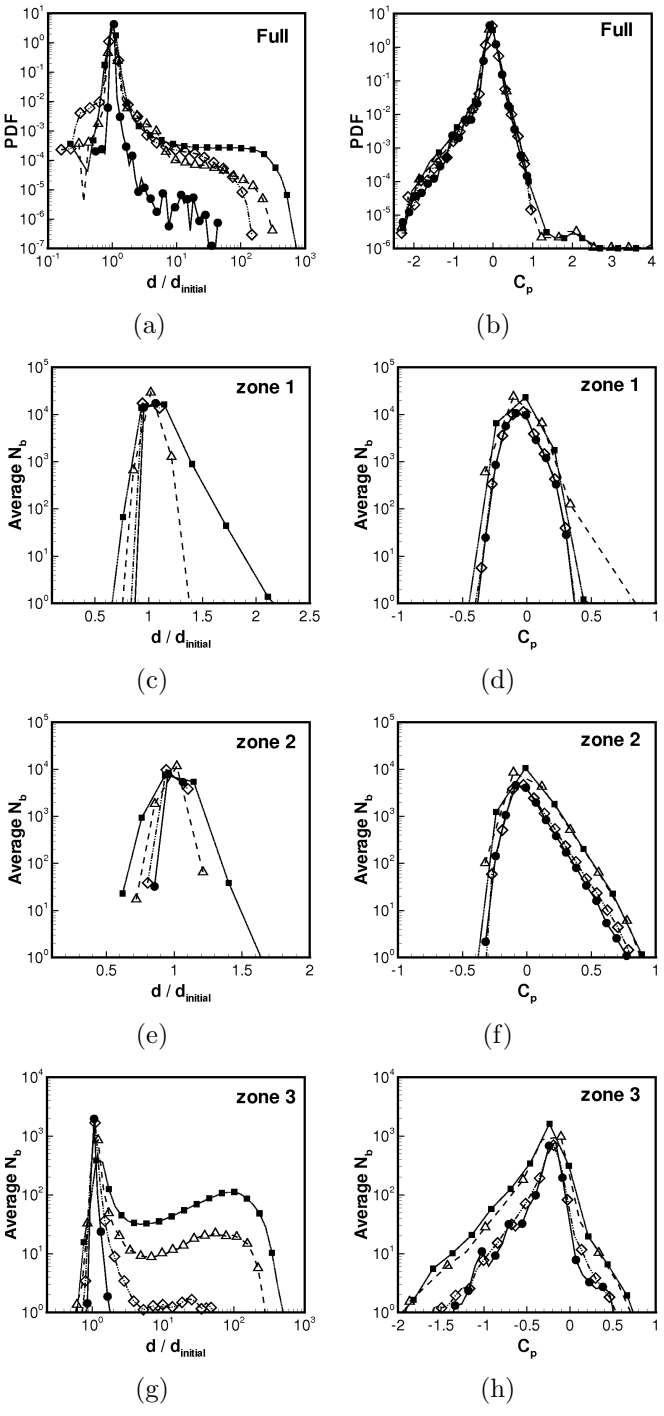

Figure 10: Effect of cavitation index σ_i on the PDFs and average number of bubbles (N_b) sampled based on the growth ratio (d/d_{initial}) and pressure coefficient C_p for case C2 ($\sigma_i = 0.4$, triangle symbols), C4 ($\sigma_i = 0.9$, diamond symbols), C5 ($\sigma_i = 1.4$, filled circles), and C6 ($\sigma_i = 0.1$, filled square): (a,b) PDF of all bubbles over the region of interest; (c,d) bubbles in zone 1; (e,f) bubbles in zone 2, and (g,h) bubbles in zone 3.

a majority of the bubbles retain their original size and are mostly insensitive to pressure variations ($d/d_{\text{initial}} \sim 1$). With lower cavitation index ($\sigma_i = 0.1$), the maximum bubble growth ratio is higher, and a small number of very large bubbles are observed near the trailing edge (giving rise to cavities on the order of 0.1-0.5 cm). This is due to the effect of lower pressure on the bubbles compared to the cases with $\sigma_i = 0.9$ and 1.4. The other important difference is on the left tail of PDF (collapse region) where the PDF of growth ratio is almost an order of magnitude larger for $\sigma_i = 0.9$ compared to $\sigma_i = 0.4$. This again indicates violent cavitation for lower cavitation index. Next we consider the behavior of bubbles in the different zones as described earlier. Figures 10c-h show average number of bubbles sampled based on the growth ratio and C_p values. In zones 1 and 2 (i.e. inside the shear layer), their is small change in the average number of bubbles versus a certain growth ratio for different cavitation indices; however, for $\sigma_i = 0.1$ and 0.4 more variation in bubble sizes were observed in both zones (figures 10(c),10(e)). Near the trailing edge, large differences in the number of bubbles with the same growth ratio are observed (figure 10(g)). For the lowest σ_i (C6), number of large bubbles observed near the trailing edge is at least an order of magnitude more than other cases (C2, C4, and C5). The highest cavitation index nearly shows no cavitation above trailing edge.

Figure 10(b) shows the PDF of C_p at bubble locations for cases C2, C4, C5, and C6 over the entire region of interest. Changing σ_i doesn't change the PDF curves sampled based on C_p appreciably; implying that the location of bubbles is not significantly affected by varying σ_i. This can also be observed in the snapshots of bubbles in figure 9. Figures 10(d), 10(f), and 10(h) show the average number of bubbles sampled based on C_p in zones 1 (near leading edge), 2 (midsection), and 3 (near trailing edge), respectively. Noticeable number of bubbles are observed in the range of $-1 \leq C_p \leq 1$. This is consistent with the experiments, wherein Liu and Katz [1] predicted cavitation inception occurs at $\sigma_i = 0.9$. These plots also indicate presence of large number of bubbles in the low pressure region for $\sigma_i = 0.1$ and 0.4. Based on the growth ratios, these are typically larger size bubbles which get attracted toward the low pressure region.

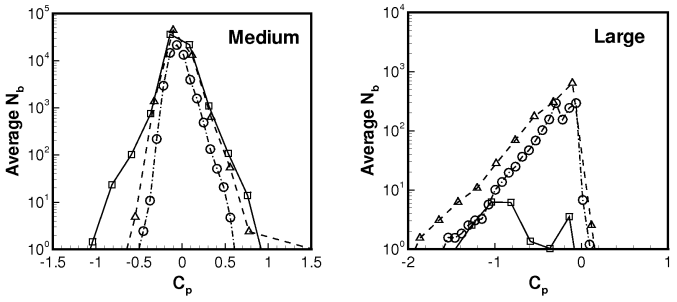

(a) (b)

Figure 11: Average number of conditionally sampled bubbles based on pressure coefficient at bubble location for case C1 (square), C2 (triangle), and C3 (circle): (a) medium size group ($0.8 < d/d_{\text{initial}} < 1.25$), (b) large size group ($1.25 < d/d_{\text{initial}}$).

Effect of Initial Bubble Size: The effect of initial bubble size (figure not shown) is also investigated by computing PDFs of growth ratio and C_p for cases C1, C2, and C3 over the entire region and in different zones [17]. It was observed that the growth of the smaller

bubbles (10 microns) is less responsive to pressure changes. A majority of them grow to about 3-4 times their original size, whereas a very few become 100 times larger. This may be attributed to the fact that smaller bubbles tend to travel with the flow (low Stokes number), thus, fewer are expected to be entrained into the lower pressure region. Larger bubbles (50 and 100 microns) can grow to very large size (10-100 times the initial size). Based on the growth ratio, 50 and 100 micron bubbles seem to be entrained in the low pressure regions in the shear layer (zones 1 and 2) and show some growth (less than twice the initial size) in these regions for $\sigma_i = 0.4$. Near the trailing edge, however, rapid growth in size is observed for these bubbles; some growing up to 50 times their original size. Correspondingly, they create cavities on the order of 0.5 cm also observed in the experiments.

Conditional Sampling and Bubble Distributions: To further characterize the sensitivity of the bubbles to imposed pressure variations, the bubbles were sampled into three groups based on their growth ratio: small ($d/d_{\text{initial}} < 0.8$), medium ($0.8 < d/d_{\text{initial}} < 1.25$), and large ($1.25 < d/d_{\text{initial}}$) bubbles. Bubbles from each group were then conditionally sampled to obtain PDFs and average number of bubbles based on C_p (figure 11) and vorticity ω distributions (not shown). Figures 11a,b show that bubbles with an initial size of 10 microns tend to remain in the medium group (i.e. $0.8 < d/d_{\text{initial}} < 1.25$), whereas larger initial size bubbles (50 and 100 micron) exhibit large growth ($1.25 < d/d_{\text{initial}}$). This indicates that bubbles with an initial size in the range of 50-100 microns are capable of predicting visible cavitation. Similar conclusions were drawn for plots based on vorticity distribution [17]. This indicates that small initial size bubbles, although sensitive to pressure fluctuations, do not tend to cluster in regions of high vorticity or low pressure. To predict cavitation inception, initial bubble sizes on the order of 50-100 micron are best suited for the present case as they tend to cluster in low pressure regions and thus can grow to large sizes. However, for other configurations, such as flow over hydrofoils, small bubbles can entrain quickly into the low pressure regions and be sensitive to rapid pressure variations.

6 Comparison of Scalar Transport and Discrete Bubble Models

In order to make a quantitative comparison of the two models in capturing small scale cavitation, we compute the temporal evolution of the *expansion ratio* predicted by the two models above the tailing edge in zone 3. The expansion ratio is a volume-averaged quantity representing the average growth in vapor fraction in a specified region compared to the initial vapor fraction and is defined as,

$$\text{Expansion Ratio} = \frac{\sum_V \phi^t_{cv} V_{cv}}{\sum_V \phi^0_{cv} V_{cv}} \quad \text{(scalar transport model)}, \tag{16}$$

$$= \frac{\sum_b V^t_b}{\sum_b V^0_b} \quad \text{(discrete bubble model)}. \tag{17}$$

Here, V_{cv} is the *cv* volume, V_b is the bubble volume, the superscripts 't' and '0' correspond to current and initial time level, and the summation (volume averaging) is carried out over

a specified volume (V); for example, above trailing edge in zone 3 where strong cavitation occurs. In both models, the initial vapor fraction is assumed to be the same. The expansion ratio thus calculated is shown in figure 12. The discrete bubble model shows larger expansion

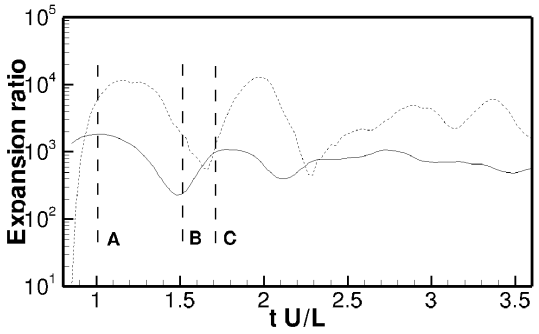

Figure 12: Average expansion ratio from scalar transport model (solid lines) and bubble cavitation model (dashed line) above the trailing edge for upstream pressure corresponding to $\sigma_i = 0.4$.

ratios compared to the scalar transport. This is mainly due to the fact the effect of pressure variations on cavitation expansion and compression is well captured on the subgrid level by the Rayleigh-Plesset equation in the bubble model. Also the bubble model shows more detailed variation for $tU/L = 2.5 - 3.5$, mainly obtained from the sub-grid dynamics of the small-scale cavitation. Both models, predict a periodic behavior of cavitation with similar frequency; however, the expansion ratio predicted by the scalar field shows a phase lag compared to the discrete bubble model. This may be due to the lack of pressure-density-velocity coupling in the present incompressible study. In addition, better estimations of the time-scale constants used in the scalar-transport model can provide a better match compared to the discrete bubble model.

Figure 13 shows the isosurface of C_p, the vapor fraction obtained from the scalar model, and instantaneous bubble distribution obtained from the discrete bubble model near the trailing edge in the side and top views. Three different snapshots are shown (corresponding to the peak and valleys of the periodic cavitation signal shown in figure 12) for an upstream cavitation index of $\sigma_i = 0.4$. Qualitatively a strong correlation is observed between the low C_p values and vapor distribution in both the scalar transport and bubble transport models.

The discrete bubble model captures the small-scale structures and the subgrid variations in bubble size. The smallest structure captured by the transport model is on the order of the local grid. The important difference between these two models is that the scalar transport model accounts for the vapor generation/destruction, whereas the bubble model predicts the growth and decay of gaseous bubbles. The scalar transport model could capture the cavitation inception on the shear layer, whereas discrete bubble model showed only a few bubbles growing in this region. This may be due to the fact that bubbles (initially being injected at the inlet and transported with flow) do not have the chance of being trapped into low pressure regions on the shear layer. These observations suggest that a hybrid model involving bubble transport (for small scale bubble dynamics) and a scalar transport model to capture large-scale cavitation features is needed. The vaporous cavitation model can be used to indicate creation of bubbles in the control volume where the C_p values become small.

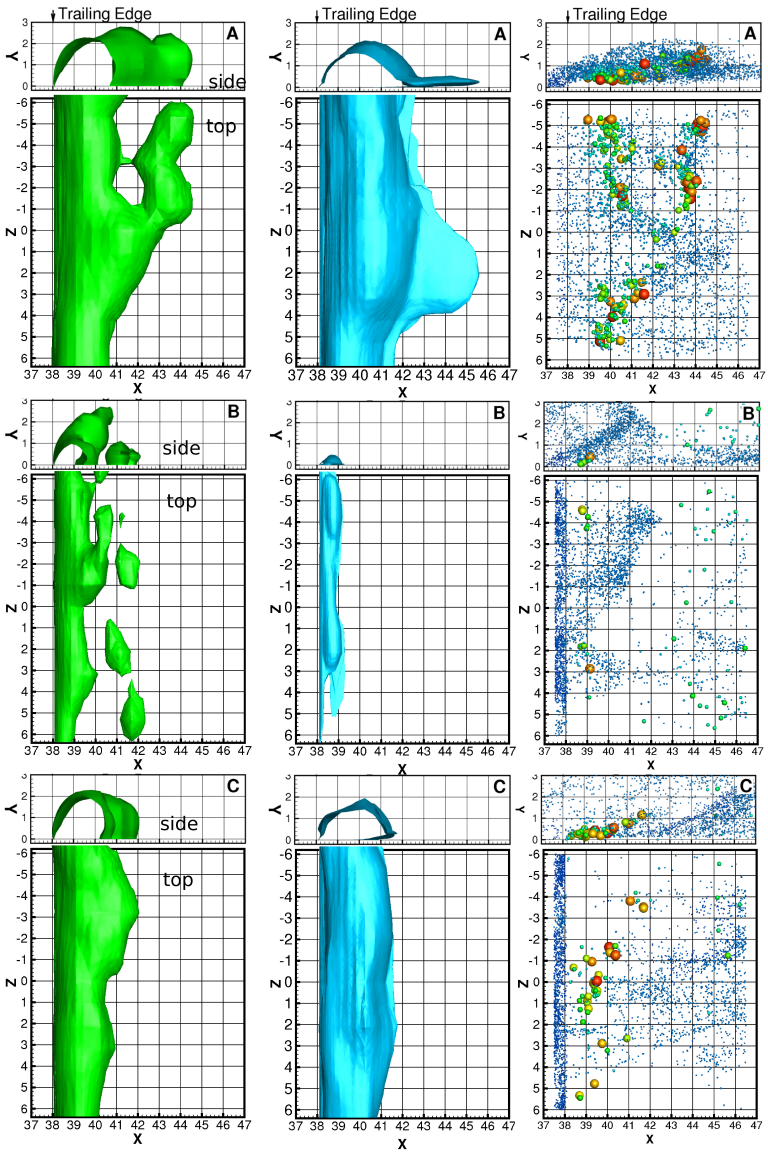

Figure 13: Instantaneous isosurfaces of $C_p = -0.25$ (left panel), and $\phi = 0.25$ (middle panel), and bubble scatter plot (right panel) for three time levels corresponding to the expansion ratio signal in figure 12: time level A (top panels), time level B (middle panel), and time level C (bottom panels). Scatter symbols are scaled to bubble size relative to the grid.

As the bubbles grow, an approach coupling the Lagrangian discrete bubbles with an Eulerian scalar field is needed to better represent the broad range of scales observed in cavitation.

7 CONCLUSIONS

We performed LES of turbulent flow over an open cavity corresponding to the experimental setup of Liu and Katz [1] at the flow Reynolds number of $170,000$. The filtered, incompressible Navier-Stokes equations were solved using a co-located grid finite-volume solver using the dynamic Smagorinsky model. Three different grid resolutions, with mainly Cartesian hexahedral elements, were considered to obtain grid independent flow statistics. The mean flowfield at the inlet section is specified from the experimental data in the symmetry plane, whereas, turbulent fluctuations were imposed at the inflow based on resolved computation of a periodic duct flow keeping the mass-flow rate and the Reynolds number the same. The flow statistics, including mean and rms velocity fields, showed reasonable agreement with the experimental data near the leading and the trailing edges. The mean pressure distribution shows two distinct features near the trailing edge: (i) a high-pressure region just upstream of the trailing edge which extends slightly into the cavity, and (ii) a low pressure region above the trailing edge. The high pressure region just upstream of the trailing edge occurs mainly due to the impingement of the shear layer onto to the trailing edge, creating a stagnation point inside the cavity. The sharp corner, downstream of the stagnation point, causes low pressure region above the trailing edge. Variations in local C_p values above the trailing edge were also investigated and showed correlations with the impingement of the shear layer vortices onto the trailing edge.

Small-scale cavitation and inception were investigated using two approaches: (i) a discrete bubble model for gaseous cavitation wherein the bubble dynamics is computed by solving the Rayleigh-Plesset and bubble motion equations using an adaptive time-stepping procedure, and (ii) a scalar transport based model for the liquid volume fraction with source and sink terms for phase change corresponding to vaporous cavitation. In both models, the effect of bubbles or vapor on the flowfield was neglected. Simulations with different values of the upstream pressure were performed by changing the cavitation index (σ_i). Both models predicted that inception occurs above the trailing edge. For $\sigma_i < 0.4$, heavy cavitation was observed above the trailing edge. The scalar transport model predicted periodic growth and decay of the liquid vapor fraction above the trailing edge owing to local variations in pressure minima. The frequency of vortex shedding as obtained based on the pressure signal is close to the theoretical prediction and also is in agreement with the experimental observations. The scalar transport model was also able to predict the cavitation inception on the shear layer for a cavitation index of 0.1. Inception on the shear layer was found to be mainly due to generation of vapor as the local pressure falls below vapor pressure.

The discrete bubble model captures the subgrid dynamics of bubbles and also shows cavitation inception occurring above the trailing edge. For low σ_i, rapid variations in bubble sizes were also observed within the shear layer. The discrete bubble model, however, could not predict large amounts of cavitation within the shear layer. Sensitivity to initial bubble size and the cavitation index were investigated in detail; it was found that 50-100 micron bubbles tend to cluster in low pressure regions and exhibit more growth. By examining the

probablity distribution functions and average number of bubbles, the inception index of 0.9 agrees well with the experimental data.

In order to make a quantitative comparison between the two models in capturing small scale cavitation, the temporal evolution of the *vapor expansion ratio*, defined as a volume-averaged quantity representing the average growth in vapor fraction in a specified region compared to the initial vapor fraction, was computed above the tailing edge. Both models indicate a periodic variation in the expansion ratio with periods corresponding to the cavitation process observed in experiment.

The present LES study indicates that the classical inception model, $C_p < -\sigma_i$, is not sufficient for description of inception dynamics in this flow. It was found that, $\overline{C}_p = -0.63$ on top of the trailing edge, whereas small-scale cavitation was observed for $\sigma_i = 0.9$ near the trailing edge in both models. The flow over an open cavity, represents a complex flow with flow separation, shear layer and interaction of the shear layer with the trailing edge. We have shown that the LES methodology together with cavitation models based on scalar and discrete bubble transport can predict the unsteady behavior of small-scale cavitation. To avoid the overprediction of eddy viscosity near the trailing edge, further analysis/development of subgrid scale viscosity models for LES in regions where the shear-layer vorticies impinge upon the trailing edge is needed. Subgrid scale models for anisotropic grids together with uniform distribution of grids near the trailing edge (making use of unstructured grids, for example) may help improve the LES predictions.

In this geometry, strong fluctuations in flow are observed on top of the trailing edge and on the shear layer. These fluctuations govern the vapor generation and bubble size variations in the cavitation models, through rapid variations in pressure and flow acceleration. The cavitation models used in the present study do not involve velocity-density-pressure coupling. In regions of vigorous cavitation (above the trailing edge), this assumption may not be accurate in the large cavity regions, and such coupling should be considered in future studies. The present study indicates that, a combination of the scalar-transport as well as discrete-bubble model for small scale cavitation is necessary capturing effects of phase transfer as well as pressure oscillations on subgrid bubble nuclei.

8 Acknowledgment

This work was supported by the Office of Naval Research (ONR) grant number N000140610697. The program manager is Dr. Ki-Han Kim. We thank Prof. Joseph Katz and Dr. Xiaofeng Liu of Johns Hopkins University for the experimental data as well as useful discussions.

References

[1] Liu, X. and Katz, J., 2008, "Cavitation phenomena occurring due to interaction of shear layer vortices with the trailing corner of a two-dimensional open cavity." Physics of Fluids, **20**(4).

[2] Arndt, R., 2002, "Cavitation in vortical flows." Annual Review of Fluid Mechanics, **34**(1), pp. 143–175.

[3] Rood, E., 1991, "Review: Mechanisms of cavitation inception," Journal of Fluids Engineering, **113**(2), pp. 163–175.

[4] Johnson, V. and Hsieh, T., 1966, "The influence of the trajectories of gas nuclei on cavitation inception," *Sixth Symposium on Naval Hydrodynamics*, pp. 163–179.

[5] Hsiao, C. and Chahine, G., 2008, "Numerical study of cavitation inception due to vortex/vortex interaction in a ducted propulsor," Journal of Ship Research, **52**(2), pp. 114–123.

[6] Hsiao, C., Jain, A., and Chahine, G., 2006, "Effect of Gas Diffusion on Bubble Entrainment and Dynamics around a Propeller," *Proceedings of 24th Symposium on Naval Hydrodynamics, Rome Italy*, vol. 26.

[7] De Chizelle, Y. K., Ceccio, S. L., and Brennen, C. E., 1995, "Observations and scaling of travelling bubble cavitation," Journal of Fluid Mechanics Digital Archive, **293**(-1), pp. 99–126.

[8] Cerutti, S., Knio, O., and Katz, J., 2000, "Numerical study of cavitation inception in the near field of an axisymmetric jet at high Reynolds number," Physics of Fluids, **12**, p. 2444.

[9] Kim, J., Paterson, E., and Stern, F., 2006, "RANS simulation of ducted marine propulsor flow including subvisual cavitation and acoustic modeling," Journal of Fluids Engineering, **128**, p. 799.

[10] Farrell, K., 2003, "Eulerian/Lagrangian analysis for the prediction of cavitation inception," Journal of Fluids Engineering, **125**(1), pp. 46–52.

[11] Alehossein, H. and Qin, Z., 2007, "Numerical analysis of Rayleigh–Plesset equation for cavitating water jets," Int. J. Numer. Meth. Engng, **72**, pp. 780–807.

[12] Wienken, W., Stiller, J., and Keller, A., 2006, "A method to predict cavitation inception using large-eddy simulation and its application to the flow past a square cylinder," Journal of Fluids Engineering, **128**, p. 316.

[13] Germano, M., Piomelli, U., Moin, P., and Cabot, W., 1991, "A dynamic subgrid-scale eddy viscosity model," Physics of Fluids A: Fluid Dynamics, **3**, p. 1760.

[14] Merkle, C. L., Feng, J., and Buelow, P., 1998, "Computational modeling of the dynamics of sheet cavitation," *Proceedings of the 3rd International Symposium on Cavitation (CAV '98), Grenoble, France.*

[15] Senocak, I. and Shyy, W., 2004, "Interfacial dynamics-based modelling of turbulent cavitating ows, Part-1: Model development and steady-state computations," International Journal for Numerical Methods in Fluids, **44**, pp. 975–995.

[16] Hsiao, C. and Chahine, G., 2002, "Prediction of vortex cavitation inception using coupled spherical and non-spherical models and UnRANS computations," *Proceedings of 24th Symposium on Naval Hydrodynamics, Fukuoka, Japan.*

[17] Sobhani, S. et al., 2010, *Numerical simulation of cavitating bubble-laden turbulent flows*, Ph.D. thesis, Oregon State University.

[18] Brennen, C., 1995, *Cavitation and bubble dynamics*, Oxford University Press, USA.

[19] Chahine, G., 1994, "Strong interactions bubble/bubble and bubble/flow," *IUTAM conference on bubble dynamics and interfacial phenomena (ed. JR Blake). Kluwer.*

[20] Apte, S., Mahesh, K., and Lundgren, T., 2008, "Accounting for finite-size effects in simulations of disperse particle-laden flows," International Journal of Multiphase Flow, pp. 260–271.

[21] Darmana, D., Deen, N., and Kuipers, J., 2006, "Parallelization of an Euler–Lagrange model using mixed domain decomposition and a mirror domain technique: Application to dispersed gas–liquid two-phase flow," Journal of Computational Physics, **220**(1), pp. 216–248.

[22] Apte, S., Shams, E., and Finn, J., 2009, "A hybrid Lagrangian-Eulerian approach for simulation of bubble dynamics," *Proceedings of the 7th International Symposium on Cavitation, CAV2009, Ann Arbor, Michigan, USA. (submitted).*

[23] Singhal, A., Vaidya, N., and Leonard, A., 1997, "Multi-dimensional simulation of cavitating flows using a PDF model for phase change," *ASME Paper FEDSM97-3272, the 1997 ASME Fluids Engineering Division Summer Meeting.*

[24] Senocak, I. and Shyy, W., 2004, "Interfacial dynamics-based modelling of turbulent cavitating ows, part-2: time-dependent computations," International Journal for Numerical Methods in Fluids, **44**, pp. 997–1016.

[25] Senocak, I. and Shyy, W., 2002, "Evaluation of Cavitation Models for Navier-Stokes Computations," FEDSM2002-31011, Proc. of 2002 ASME Fluids Engineering Division Summer Meeting Montreal, CA.

[26] Mahesh, K., Constantinescu, G., and Moin, P., 2004, "A numerical method for large-eddy simulation in complex geometries," J. Comput. Phys., **197**(1), pp. 215–240.

[27] Mahesh, K., Constantinescu, G., Apte, S., Iaccarino, G., Ham, F., and Moin, P., 2006, "Large-eddy simulation of reacting turbulent flows in complex geometries," J. Applied Mech., **73**, p. 374.

[28] Moin, P. and Apte, S., 2006, "Large-eddy simulation of realistic gas turbine-combustors," AIAA Journal, **44**(4), pp. 698–708.

[29] Apte, S., Mahesh, K., Moin, P., and Oefelein, J., 2003, "Large-eddy simulation of swirling particle-laden flows in a coaxial-jet combustor," International Journal of Multiphase Flow, **29**(8), pp. 1311–1331.

[30] Pierce, C. and Moin, P., 1998, "Large eddy simulation of a confined coaxial jet with swirl and heat release," AIAA Paper, **2892**.

[31] Liu, X. and Katz, J., 2006, "Instantaneous pressure and material acceleration measurements using a four-exposure PIV system," Experiments in Fluids, **41**(2), pp. 227–240, URL `http://dx.doi.org/10.1007/s00348-006-0152-7`.

[32] Martin, W., Naudascher, E., and Padmanabhan, M., 1975, "Fluid-dynamic excitation involving flow instability," Journal of Hydraulic Division, **101**, p. 681.

[33] Blake, W., 1986, *Mechanics of flow-induced sound and vibration*, Academic, New York, 1986.